Avoiding Shading Losses in Concentrator Photovoltaics Using a Soft-Imprinted Cloaking Geometry

Stefan W. Tabernig, Anastasia H. Soeriyadi, Udo Römer, Andreas Pusch, Dimitry Lamers, Matthias Klaus Juhl, David N. R. Payne, Michael P. Nielsen, Albert Polman, and Nicholas J. Ekins-Daukes

***Abstract*—Shading losses are a longstanding obstacle in photovoltaic devices, particularly in concentrator photovoltaics, where the tradeoff between shading and resistive losses limits the concentration at which the highest power conversion efficiency is achieved to values far below the capabilities of concentrator optics. Here, we demonstrate a simple and scalable fabrication method that enables large front metal coverage while keeping shading losses to a minimum. Soft-imprint lithography is used to create trenches in a transparent polymer above the metal contacts, enabling cloaking via refraction at a range of angles near normal incidence. Using optical characterization techniques, we first confirm that the metal contacts are indeed optically cloaked. We then demonstrate an increase in short-circuit current density from 29.95 to 39.12 mA/cm^2 for a Si solar cell with 25% front metal coverage before and after patterning, respectively. We investigate the angular performance of the trench pattern and further demonstrate how such a cloaking strategy could be implemented in concentrator photovoltaics to enable efficiency peaks at concentrations beyond 1000 suns.**

***Index Terms*—Concentrator photovoltaics (CPV), contact cloaking, high-efficiency photovoltaics, resistive loss, shading loss, soft-imprint lithography, transparent contacts.**

Manuscript received 18 March 2022; revised 22 May 2022; accepted 7 June 2022. Date of publication 22 June 2022; date of current version 19 August 2022. This work was supported in part by the NSW Node of the Australian National Fabrication Facility, in part by the Australian Government through the Australian Renewable Energy Agency, the Australian Centre of Advanced Photovoltaics, in part by the Australian Government through the Australian Research Council's DECRA program (No. DE210100453), in part by the Research and Prototype Foundry Core Research Facility at the University of Sydney, and in part by the Australian National Fabrication Facility. *(Corresponding authors: Stefan W. Tabernig; Albert Polman; Nicholas J. Ekins-Daukes.)*

Stefan W. Tabernig is with the Center for Nanophotonics, NWO-Institute AMOLF, 1098 XG Amsterdam, The Netherlands, and also with the School of Photovoltaic and Renewable Energy Engineering, University of New South Wales, Sydney, NSW 2052, Australia (e-mail: s.tabernig@amolf.nl).

Anastasia H. Soeriyadi, Udo Römer, Andreas Pusch, Michael P. Nielsen, and Nicholas J. Ekins-Daukes are with the School of Photovoltaic and Renewable Energy Engineering, University of New South Wales, Sydney, NSW 2052, Australia (e-mail: anastasia.soeriyadi@unsw.edu.au; u.romer@unsw.edu.au; a.pusch@unsw.edu.au; michael.nielsen@unsw.edu.au; nekins@unsw.edu.au).

Dimitry Lamers and Albert Polman are with the Center for Nanophotonics, NWO-Institute AMOLF, 1098 XG Amsterdam, The Netherlands (e-mail: d.lamers@amolf.nl; a.polman@amolf.nl).

Matthias Klaus Juhl and David N. R. Payne are with the School of Engineering, Macquarie University, Sydney, NSW 2109, Australia (e-mail: mattias.juhl@unsw.edu.au; david.payne@mq.edu.au).

Color versions of one or more figures in this article are available at https://doi.org/10.1109/JPHOTOV.2022.3182277.

Digital Object Identifier 10.1109/JPHOTOV.2022.3182277

I. Introduction

In recent years, electricity generation from mainstream photovoltaic (PV) technologies, dominated by rooftop solar and utility scale solar plants, has established itself as one of the cheapest sources of electricity [1], considerably cheaper than alternative nonrenewable energy sources (coal, gas, and nuclear) [2]. Aided by this, formerly niche applications of PV, such as building-integrated PV [3]–[5], vehicle-integrated PV [6], and space PV [7]–[9], have also experienced considerable growth in recent years. Besides these, concentrator photovoltaics (CPV) [10] remain promising for utility scale power generation, as its levelized cost of electricity (LCOE) [11] is predicted to drop rapidly and may soon reach the LCOE of conventional PV in high-irradiation regions [12].

While CPV requires more elaborate infrastructure than conventional PV, it offers a range of benefits. First, the fundamental detailed balance efficiency limit is significantly higher due to a logarithmic gain in open-circuit voltage (V_{OC}) as a function of the concentration factor [13]. So far, the current world record for CPV is 47.1% (143 suns), which is 7.9% absolute above the 1-sun efficiency of the same device [14]. This is also 7.6% higher than the currently best performing nonconcentrator solar cell (39.5%) [15]. Second, CPV requires much less active solar cell area as it employs concentrator optics to focus light onto a small cell area. Thus, with increasing concentration, the cost of the cell becomes less significant compared with the cost of the overall system. This allows for large-scale implementation of solar cells that are based on highly efficient albeit expensive technologies, such as III-V solar cells. Furthermore, CPV can be combined with solar thermal concentrator/storage architectures [16] to make more efficient use of sub-bandgap infrared radiation and, thus, increase the overall system efficiency beyond the efficiency of the CPV subsystem alone.

The concentration factors at which the highest efficiencies are achieved are currently limited to values on the order of 100 [14], [15]. For higher concentration, the efficiency decreases due to a rise in resistive losses that scale quadratically with the current density in the front metal contact grid [17]. To counteract this, the front metal grid coverage is often in the range of 10–15% for concentrator solar cells [18], compared with only 4% for conventional solar cells [18]. While this improves extraction, it also increases the optical shading of the solar cell, resulting in

This work is licensed under a Creative Commons Attribution 4.0 License. For more information, see https://creativecommons.org/licenses/by/4.0/

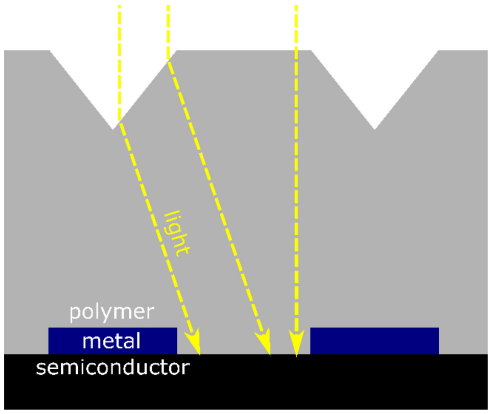

Fig. 1. Schematic representation of refractive contact cloaking (not to scale). Normal incident light is refracted by triangular polymer trenches onto the underlying semiconductor absorber and away from the metal contacts.

exchanging one loss against another. Hence, the final CPV front contact grid designs are usually derived from a tradeoff between shading losses and resistive losses, with efforts to push the highest efficiency region to a concentration closer to 1000 suns requiring avoiding this tradeoff.

This work proposes a strategy to overcome this tradeoff by making the front metal grid invisible to the incident light. We achieve this by coating a transparent, ultravoilet (UV)-curable polymer onto the front of a solar cell and subsequently patterning it. Following geometric optics, the patterned structures redirect light onto the semiconductor absorber and away from the metal grid and, thus, eliminate the effect of shading to increase the short-circuit current density (J_{SC}). The angular optical performance of the new design enables concentration values of well above 1000. We, therefore, demonstrate a path toward 1000-fold concentration for a front metal coverage of 25%, with low shading losses of only 1.8%.

Similar approaches toward effectively transparent contacts have been attempted in the past, but they either rely on a more complex fabrication procedure [19]–[22], which are difficult to upscale [21], or involve potentially parasitic reflection from metals [20], [23]–[26]. While a few [19]–[21] have looked into the dependence on the illumination angle, the overall shading as a consequence of concentration geometry and angular performance has only been discussed for one of these approaches [25], [26]. While the different approaches used in these studies yield different angular dependencies of the external quantum efficiency (EQE), we find that the best devices lie within the same range as our device at normal incidence, although our device has the highest front metal coverage reported.

II. Design

Fig. 1 shows the general design of the proposed structure. The underlying semiconductor absorber, along with the front metal grid, is covered by a transparent polymer that contains triangular trenches aligned with the metal contacts. The light that would reach the metal contacts in a planar structure now is refracted toward the midpoint between the contacts and, thus, reaches the semiconductor absorber. This requires a certain refractive index contrast between the air and the polymer, adding a loss channel due to reflection. However, a glass(/polymer)–air interface is standard for any solar cell that is embedded in a module, and the proposed layer structure should, thus, be seen as the first piece of the solar module instead of the solar cell alone.

While multiple patterns of lines of various widths and pitches were investigated, a fixed width (10 μm) and pitch (40 μm) form the core of this study, which corresponds to 25% shading. We note that to achieve this 25% metal coverage, we have already fixed a range of parameters for our final structure. The last remaining free parameter, the separation between the top of the metal contacts and the bottom of the polymer trenches (d), is chosen such that the light refracted at the bottom of the trench misses the contact and that the light refracted at the top of the trench does not hit a neighboring contact. All dimensions and relevant parameters are summarized in the Appendix, as shown in Fig. 8 and Table I.

III. Fabrication

Substrate conformal soft-imprint lithography (SCIL [27]) in combination with a UV-curing transparent polymer (OrmoComp [28]) was used to create the refractive layer. This entails the fabrication of a Si wafer that contains the pattern for the polymer (master wafer), a polydimethylsiloxane (PDMS) mold (stamp), and subsequent patterning of the actual sample (see Fig. 2). The master wafer was made from a (100) Si wafer and patterned via KOH wet etching [see Fig. 2(a)]. The anisotropic nature of KOH wet etching results in an exposure of the (111) facet, which is at an angle of 54.74° toward the (100) facet. By masking the Si wafer appropriately, triangular trenches inside the Si [see Fig. 2(b)] were created and subsequently filled with PDMS.

The hardened PDMS was peeled off and became the stamp pattern for the sample fabrication [see Fig. 2(c)]. To transfer the pattern onto the samples, we combined SCIL and UV lithography by using the transparent PDMS stamp. The stamp was brought into contact with the liquid OrmoComp polymer and aligned with the metal contacts [see Fig. 2(d)]. Subsequent UV exposure and stamp removal yielded the finished sample [see Fig. 2(e)]. We refer to Appendix A for more details on the complete fabrication sequence.

Fig. 3(a) shows a detailed scheme of the master wafer fabrication. These steps yield a Si wafer with a grooved pattern, as shown in Fig. 3(b)–(d). The trenches are visible at the top of the wafer and the edges appear clean. The top edge appears to have some residue, which most likely comes from the cleaving of the sample that was necessary to obtain a cross-sectional image. Thin lines are visible inside the trenches, corresponding to steps in the (111) Si plane, commonly observed during Si KOH etching. Those step features are negligible as they will not affect the intended light refraction. The region imaged in the scanning electron microscope (SEM) is one of many fields of varying dimensions that we introduced onto the Si surface to test the stamp fabrication process. The different fields can be seen as separated squares on the PDMS stamp, as shown in Fig. 3(e).

The first step of the sample fabrication entails the deposition of a polymer spacer layer on top of the sample/solar cell. This introduces the required metal–trench separation (d). Then, the

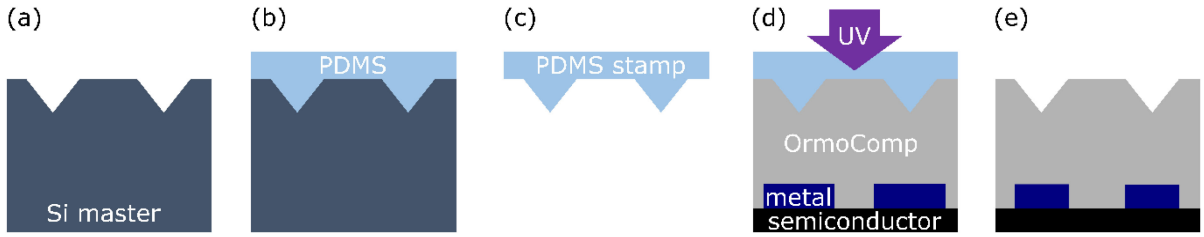

Fig. 2. Main fabrication steps toward a solar cell with the patterned polymer on top. Polymer in gray, metal contacts in yellow, and absorber layer in black. (a) Wet etching of trenches into a Si wafer with KOH to get the Si master. (b) Filling up of the trenches with PDMS to form the pattern for the PDMS stamp. (c) Peeling-off of the PDMS stamp from the Si master. (d) Si solar cell covered with OrmoComp (liquid polymer), stamp in contact with OrmoComp and aligned with the metal grid. Subsequent UV exposure hardens the polymer. (e) Final patterned sample after separation from the PDMS stamp.

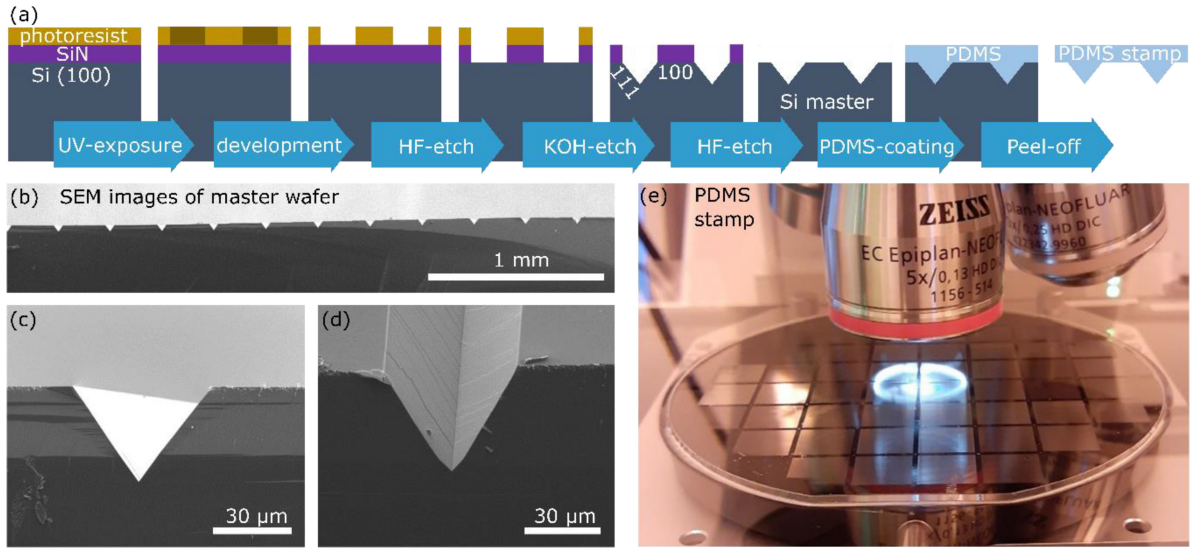

Fig. 3. (a) Detailed scheme of the required fabrication steps for a Si master wafer. PDMS in light blue. The photoresist-SiN_x-Si(100) structure experiences masked UV exposure, development, HF etching of SiNx, photoresist removal, KOH etching of Si, SiNx-removal via HF etching, PDMS coating, and PDMS peel-off to obtain the stamp. (b) SEM cross-sectional image of Si master. (c) Close-up of cross section of a single trench. (d) 45°-view of trench. (e) Photograph of the finished PDMS stamp under a microscope objective. The different squares are 1 cm^2 in size and contain trenches of various widths and pitches. Note: SEM images in (b), (c), (d) were taken on a test field with larger pitch and trench width than used for the sample fabrication later on.

planar polymer layer is covered with the polymer layer that is to be patterned. For the patterning, one of the stamp fields was selected and brought into contact with the liquid polymer and the sample. The contacts and trenches are aligned by minimizing Moiré interference and sample brightness via rotation and translation of the samples. This is followed by UV exposure and stamp-sample separation to obtain the final samples. More details can be found in Appendix A.

The patterned samples were first investigated with SEM and optical microscopy. Fig. 4(a) shows an SEM cross-sectional image of a sample with metal contacts and the patterned polymer on top. The interface between the first and second polymer layers cannot be distinguished, indicating that no interface defects, such as voids, were generated. Furthermore, the polymer was coated conformally around the metal contacts despite the roughness of the evaporated contacts.

In Fig. 4(b), we can see an optical microscope image that shows that the metal contacts are indeed cloaked by refraction by the polymer pattern. This is highlighted by the air bubble defect in the image. The metal (Au) finger is clearly visible there, as an air bubble replaced the polymer during the imprint and exposure stage. We note that Au contacts were used for samples intended for optical characterization, while we used Al contacts for solar cells. Across the rest of the sample, two dark lines are seen on each side of the trench walls of the cloaked metal contacts. The lower intensity compared with the flat section is due to the difference in backscattered light depending on whether light hits the trench or the flat surface. The light that hits the planar regions experiences an ordinary reflection either at the polymer surface or at the semiconductor surface, while light that reaches the trenched region is refracted onto the semiconductor and can only couple out via a planar surface as it is totally internally reflected by the trench walls.

The elimination of shading can also be observed by naked eye. Fig. 4(c) and (d) shows a Si cell with a planar and a patterned polymer layer, respectively. Since the pattern directs light away from the metal and onto the absorber, the reflection of the sample is reduced, making it appear dark blue due to the antireflection coating (on top of the Si cell). Air bubble defects can also be observed in both samples. These can arise when the PDMS

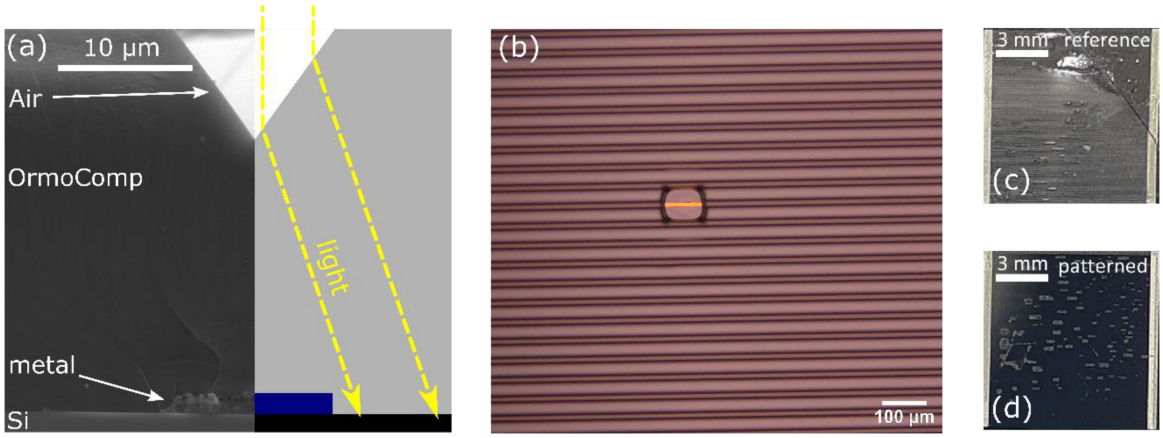

Fig. 4. SEM and microscope characterization of patterned samples. (a) Direct comparison between a cross-sectional SEM image of the fabricated geometry and schematic design from Fig. 1. (b) Optical microscope image of the top view of a patterned sample with an air bubble defect. (c) Photograph of metal (Al) covered Si solar cells with planar polymer on top. Top right: Crack through cell from fabrication. Centre: air bubble defects. (d) Photograph of cell from the same batch but with patterned polymer on top. Air bubbles appear gray.

stamp is brought into contact with the liquid polymer before UV exposure and translate into imperfectly uniform polymer coverage. This effect can be avoided if the SCIL process is further optimized for large throughput processing.

Note that from the master fabrication to the finished patterned solar cell, we mainly used well-established scalable processes and materials. Furthermore, the most crucial step, the trench–contact alignment, can be done by minimization of reflection by naked eye. For large-scale applications, automated reflection intensity monitors can optimize for minimum reflection. Additionally, the feature resolution limit for SCIL is 6 nm [27], well below the resolution requirements for the refractive trenches discussed in this work. One potential bottleneck could be the use of OrmoComp (relatively expensive) as the polymer on a large scale, although this material might be replaced by a range of other less expensive UV-curing transparent polymers. Polymethylmethacrylate (PMMA) is such an interesting candidate for the replacement of the polymer, provided cross-linking molecules that allow for PMMA as a negative UV resist are used [29].

IV. Optical Characterization

To investigate the optical performance of the transparent polymer layer, transparent quartz samples with Au grids and the patterned polymer on top were fabricated. Additionally, two reference samples were used, the first consisting of a quartz sample, with a metal grid, and a planar polymer. The second consisting of a pure quartz sample. These references represent the best (100% transparency) and worst (0% transparency) cases that a patterned sample can attain in our comparison. The transparency describes the fraction of incident light that is refracted away from the metal. Note that the reference for the best case (100% transparency) is a bare quartz sample that does not include a planar polymer layer on top, as this corresponds to a comparison of the sample before and after deposition of our structure.

To assess the quality of the transparency (Q_T) under normal incidence, we use integrating sphere (IS) measurements to measure the reflection of the sample [see Fig. 5(a)]. Then, we use the measured absorption of the sample combined with the known spectral dependence of parasitic absorption by Au to assess the angular performance of our fabricated samples [see Fig. 5(b)–(d)]. Additional data for reflection, resolved for different reflection angles, can be found in the Appendix (see Fig. 11).

The reflection (R) was measured with the samples mounted at the back of the IS, opposite to the inlet port. To get an adequate comparison between the different samples, performance values were derived from the range between 700 and 800 nm, for which all materials on the samples are either good reflectors (Au) or nonabsorbing (OrmoComp, quartz). Fig. 5(a) shows the comparison between the two references and the patterned quartz sample. The reflection of the patterned sample ($R_{\mathrm{patterned}}$) is similar to that of the fully transparent quartz reference (R_{quartz}). For wavelengths shorter than 550 nm, the patterned cell shows even lower reflection than the quartz sample. This is due to a decrease in reflection and an increase in absorption of Au in that range. The same trend is much stronger for the sample with a planar polymer coating (R_{planar}). Further toward the UV range, below 365 nm, the polymer strongly absorbs, leading to a dip in reflection for the two polymer-coated samples (see SI for optical data). Considering all this, the range between 700 and 800 nm is the most appropriate range for the quantification of the transparency of the patterned sample, as Au is an almost perfect reflector in that range. This yields $Q_T = 95.2\%$, calculated using the expression

$$Q_T\ (\lambda) = \frac{R_{\mathrm{planar}}\,(\lambda) - R_{\mathrm{patterned}}\,(\lambda)}{R_{\mathrm{planar}}\,(\lambda) - R_{\mathrm{quartz}}\,(\lambda)}. \tag{1}$$

An analogous set of measurements was conducted with the samples in the transmission configuration of the IS, and the corresponding analysis can be found in the Appendix.

As in a solar concentrating geometry, sunlight will hit the solar cell at a range of angles; the full angular performance of the structure was investigated, as shown in Fig. 5(b)–(d). The IS measurements were performed with samples mounted in the center of the sphere. The light that was collected in

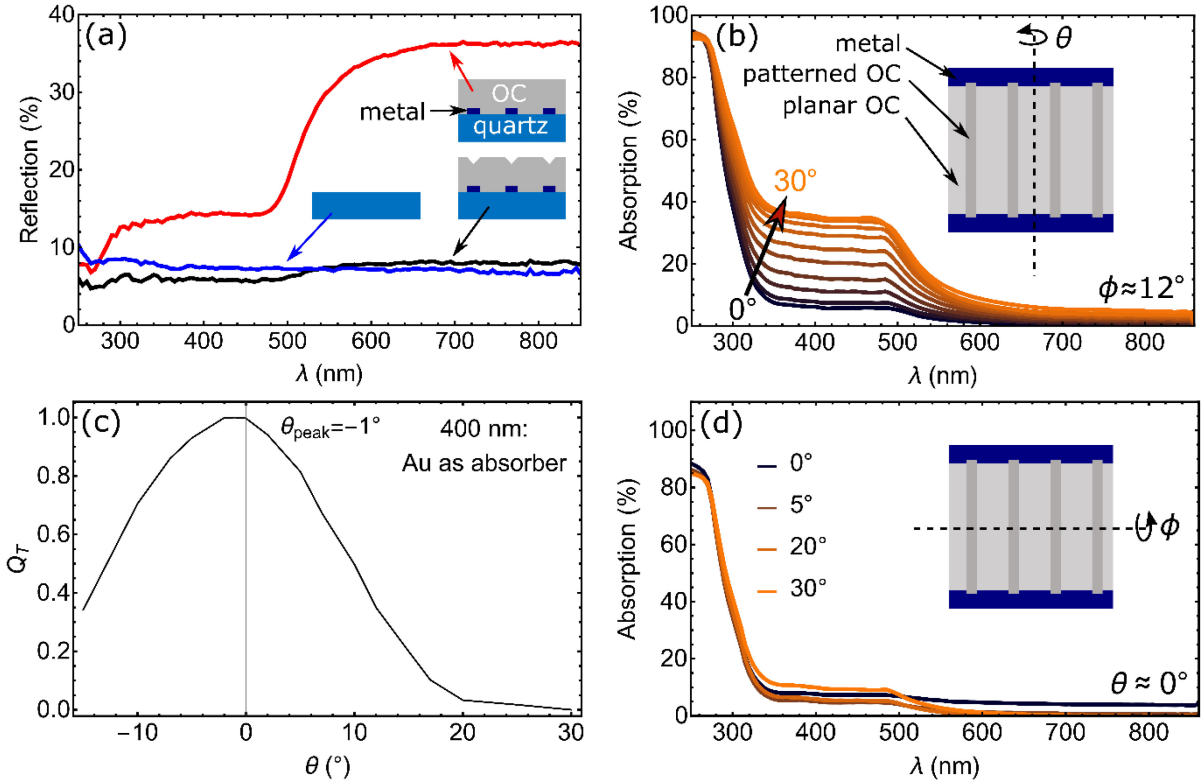

Fig. 5. Optical characterization of patterned samples. (a) Comparison of total reflection among a patterned quartz sample with Au grid (black), a planar sample with Au grid (red), and a bare quartz sample (blue). In this case, the metal (Au) coverage was 30%. (b) Total absorption by the patterned quartz + Au-finger sample for a range of AOI (θ). The inset drawing shows the rotation axis (parallel to contacts). These measurements were conducted with ϕ <12°. The change in graph color from black toward orange corresponds to an increase in angle from 0° (black) to 30° (orange). (c) Change in quality of the transparency (Q_T) as a function of angle θ at 400 nm wavelength. (d) Total absorption by the patterned quartz + Au-finger sample for various AOI (ϕ). The inset drawing shows the rotation axis (perpendicular to contacts).

this measurement mode corresponds to the sum of reflected light (R) and transmitted light (T) for all angles. From this, we deduced the absorption of the measured sample, using $A = 1-R-T$. As the investigated sample contained quartz (absorbing below 200 nm), OrmoComp (absorbing below 365 nm), and Au (strongly absorbing below 550 nm), we used this measurement mode to determine parasitic absorption within the Au layer, by investigating the range between 365 and 550 nm. Furthermore, the sample was slightly (>12°) tilted along ϕ (the rotation axis perpendicular to the Au contacts) to prevent the specular reflection from escaping through the inlet for small sample rotation angles of θ<12°.

Fig. 5(b) shows the parasitic absorption by the Au grid for rotations around the rotation axis parallel to the Au contacts (θ) in the range 0°<θ<30°. Rotation around this axis changes the optical paths such that light is directed onto the Au contacts, thus reducing the beneficial effect of the trenches. The data show that the absorption in the system increases gradually with increasing angle θ and saturates toward $\theta = 30°$. Between 365 and 550 nm, the absorption is dominated by the increased absorption in Au in this range, and for wavelengths shorter than 365 nm, the polymer also contributes. Note that the absorption saturates at a value that corresponds well with the Au coverage and it shows a wavelength dependence that agrees well with the optical constants of Au.

Fig. 5(c) summarizes the data from Fig. 5(b) by calculating the dependence of Q_T on θ from the absorption values (A) taken at 400 nm. With the best performance at $\theta = 0°$ and worst performance at $\theta = \theta_{\max}$, we can calculate $Q_T(\theta)$ from (2), for $\lambda = 400$ nm

$$Q_T\ (\theta) = Q_T\ (0)\ \frac{A\,(\theta_{\max}) - A\,(\theta)}{A\,(\theta_{\max}) - A\,(0)}. \tag{2}$$

Fig. 5(c) also includes the data measured for the rotation in the opposite direction. From the peak position, it becomes apparent that there was a slight offset of 1° from the alignment of the sample in the IS. In general, the data show that the transparency vanishes at incoming angles θ larger than 20°. However, there is a plateau of high transparency for small angles as the trench width is wider than the Au width. This tolerance to rotation along θ can be improved if the trenches are made even wider relative to the contacts. In a first approximation, which neglects the impact of extended trenches with regard to refraction onto adjacent contacts, a 40% wider trench compared with the contact width would cause the plateau to extend to $\theta = 5°$ (see Appendix, for an analysis of the influence of the trench width relative to the contact width).

Finally, Fig. 5(d) shows the absorption with respect to rotation around ϕ. For rotation along ϕ, the absorption by the Au contacts does not increase toward larger angles. Since the trenches run

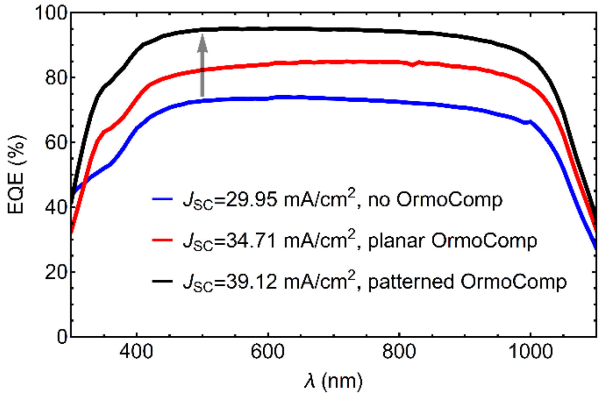

Fig. 6. EQE as a function of wavelength. Curves shown for Si solar cells with front Al-grid, pyramidal texture, and SiN_x antireflection coating. Performance of bare cell (blue) improves significantly after deposition of planar polymer (red) and makes another jump with the patterned polymer (black). The gray arrow indicates the fabrication order.

perpendicular to this rotation direction, no significant degradation in performance as a function of angle of incidence (AOI) is expected up to the Brewster angle. The absorption at $\phi = 0°$ appears slightly higher because of the fact that θ was also set to 0°, and hence, the specular reflection was lost through the entrance and not collected by the IS.

V. Electronic Characterization

So far, the optical data suggest that shading was eliminated almost entirely for the investigated samples at small AOI. To confirm that this also translates into stronger light absorption in a solar cell, we compared the EQE of cells before and after deposition of the transparent polymer. The samples used were textured silicon solar cells with a SiN_x antireflection coating and a 25% Al metal coverage (see Appendix A for fabrication details). While the intended application of the patterned polymer coating is on top of III-V concentrator solar cells, Si solar cells serve as a relevant platform for an investigation of the improvements in EQE due to contact cloaking.

Fig. 6 shows the improvement of the normal incidence EQE due to the introduction and patterning of the polymer. The EQE measurement sampled an accurate ratio of metal contacts and absorber regions to represent the metal coverage of 25%. The data for a sample without the polymer and with the patterned polymer were measured on the same sample; the data for the sample with the planar polymer layer were obtained from a different sample of the same batch.

We can see how the EQE increases just by the introduction of the planar polymer layer. The reason for this is that this extra layer has a refractive index ($n = 1.564$) between that of Si and air and, hence, lowers the overall sample reflection. Furthermore, as the cell has a pyramidal texture on top, the polymer also acts as a trapping layer for light that is scattered into shallow angles from the Si absorber or the Al contacts. The drop in EQE below 365 nm is related to the absorption of the polymer. Furthermore, the gradual decrease in the EQE improvement compared with the reference that occurs below 700 nm is possibly associated to increased absorption in the metal grid from enhanced light trapping.

The EQE of the patterned sample peaks at 95.0%. To get a value for Q_T, we use (A5) and first take into account that a fraction of 70% of the patterned sample's polymer surface is planar and that the loss from a planar OrmoComp reflection is 3.4%. The reflection of light scattered out by reflecting off two trench walls, taking into account the reflection angle of first (54.7°, $R_1 = 7.9\%$) and second (15.8°, $R_2 = 4.9\%$) reflections, contributes to the overall reflection by $(7.9\%) \times (4.9\%) \times 0.3 = 0.1\%$. The remaining 1.5% EQE loss can be attributed to fabrication defects associated with the polymer trenches and could be avoided by using further optimized patterning procedures and tools. This means that the shading was reduced from 25% to 1.5% and we can calculate the quality of the transparency in the electronic experiments to be $Q_T = 1 - \frac{0.015}{0.25} = 0.94$.

We have derived Q_T for planar samples in optical (95.2%) and textured samples in electronic (94.0%) experiments, as well as established the angular dependence of Q_T. The difference between these Q_T values can partially be explained by a difference in spot size and shape in optical and electronic measurements. Furthermore, different samples were used in the two experiments; therefore, a sample-to-sample deviation is also possible.

VI. Prospective Performance in a Concentrator Setup

Using the results obtained in Section V, we can estimate the level of solar concentration at which the cloaking trenches perform as desired. Assuming negligible influence from variation in ϕ, the effective shading (S_{eff}) can be calculated by integrating $Q_T(\theta)$ over a chosen θ range. The derivation of (3) can be found in the Appendix

$$S_{\text{eff}}(\theta) = S\left(1 - \frac{1}{\sin(\theta)}\int_0^{\theta} Q_T(\theta')\cos(\theta')\,d\theta'\right). \quad (3)$$

Fig. 7(a) shows the maximum concentration that we can achieve depending on the concentration pattern [see Fig. 7(b) and (c)]. The Brewster angle of the polymer is 57.4°, which marks the upper limit for ϕ such that increased reflection does not lower the performance of the cell. We can see that small θ angles can be sufficient to reach 1000 suns concentration, if a large angular range along ϕ is concentrated onto the cell. In fact, for full exhaustion of the Brewster-limited ϕ range, a θ range of up to 2° is already sufficient to reach 1000-fold concentration [see Fig. 7(b)]. Combining this with the analysis of the angular performance, as shown in Fig. 5(c), we get an effective shading of 1.8% for this choice of angles. Furthermore, we show that if one were to increase both angles at the same rate to get a circular concentration pattern [see Fig. 7(c)], 1000-fold concentration could only be reached at S_{eff} beyond 5.0%. The second y-axis, as shown in Fig. 7(a), outlines the potential absolute efficiency gain that one could expect for a single-junction GaAs solar cell, according to the detailed balance limit (see Appendix for the calculation). These gains would be even larger if calculated for the current world record six-junction solar cell [14].

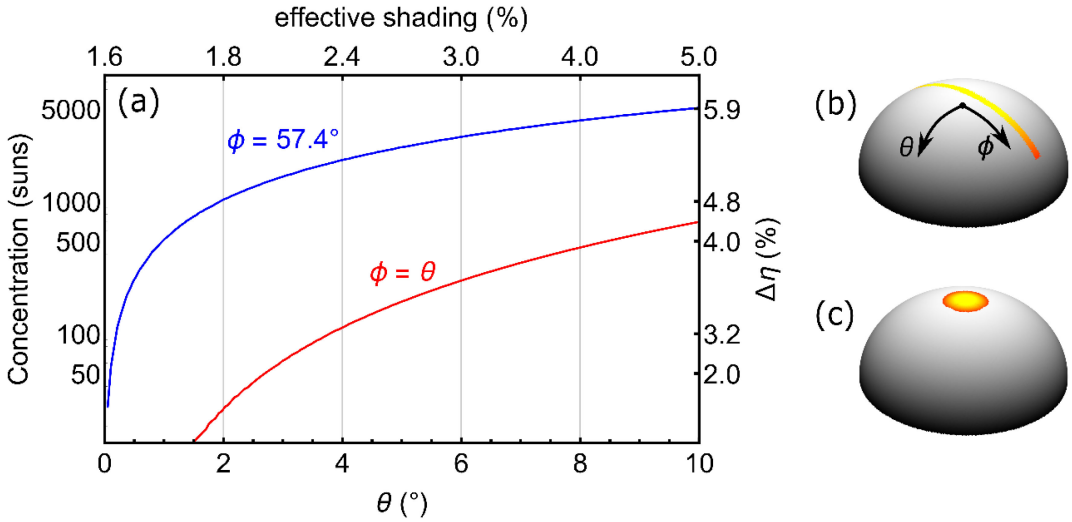

Fig. 7. Prospects for integration into a CPV setup. (a) Achievable concentrations as a function of the limiting angle θ, plotted for values of $\phi = 57.4°$ (blue) and for $\phi = \theta$ (red). The total effective shading associated with a given maximum angle θ is shown along the top x-axis. The right y-axis shows the calculated absolute efficiency gain for a given concentration. (b) Illustration of the concentration pattern for 1000 suns at $\varphi = 57.4°$ and $\theta = 2°$. The yellow-to-red color gradient corresponds to the deviation from 0° incidence. (c) Illustration of the concentration pattern for 1000 suns with $\phi = \theta$.

We show the visualization of the concentration pattern necessary for 1000 suns at the lowest possible S_{eff} in Fig. 7(b). The solar cell sits in the center of the hemisphere and is exposed to light across that hemisphere. Instead of the sun occupying only a small area of the hemisphere, we see the extend of the solid angle that 1000 suns require on a hemispherical surface. In this case, the area is shaped such that it is limited by the Brewster angle (57.4°) in ϕ-direction and by 2° along θ. This slice of the hemisphere surface minimizes the effective shading and, hence, would lead to the best possible performance for a cell with the transparent contact design we propose. Fig. 7(c) visualizes what 1000 suns concentration look like for a circular concentration pattern, and it becomes obvious that this extends much further into the unfavorable θ-direction.

The concentration pattern, as shown in Fig. 7(b), can be achieved using a trough concentrator [30], [31] whereby light is focused along one direction only and, hence, corresponds to 1 sun along θ such that concentration along ϕ would allow for 252-fold concentration. Higher concentration can be achieved by also focusing light along θ to achieve the proposed concentration pattern for 1000 suns.

At this point, it should be noted that another important aspect is the stability of the used polymer under such large concentrations in terms of heat and UV exposure. This should be investigated prior to the experimental demonstration of such cells under concentrated sunlight.

VII. Conclusion

In this article, we have demonstrated a path toward the reduction of shading losses in solar cells, with a focus on allowing for much higher front contact coverage, that can minimize resistive losses in concentrator solar cells. We discussed the full fabrication procedure, optical properties, and electronic output for a V-groove polymer coating geometry that cloaks the metal contacts on a solar cell.

SEM images showed good agreement with design and optical images indicate that the patterned polymer cloaks the metal contacts effectively. This was further confirmed by optical characterization of quartz samples with Au grids that were made effectively transparent. From this, we derive the first estimate for the quality factor Q_T to be 95.2%.

We also investigated the performance under varying angles of incidence and find that Q_T only decreases by rotation around the axis that is parallel to the metal contacts (θ). Rotation around the axis that is normal to the metal contacts (ϕ) does not affect Q_T.

Electronic measurements show that the shading loss of the EQE from a dense metal grid can be recovered almost completely. The electronic data also yield a second estimate for Q_T, which is 94.0%.

Finally, we take Q_T and its angular dependence into account to come up with a simple concentration geometry that would allow for concentration intensities of 1000 suns while mitigating the shading/resistance loss tradeoff almost completely. In fact, the proposed structure can translate a metal coverage of 25% into an effective shading of only 1.8% at 1000 suns.

Considering the potential gains in conversion efficiencies at higher concentrations that this approach enables (4.8% for a single-junction GaAs cell), we have outlined a path beyond 50% laboratory power conversion efficiencies for multijunction solar cells [14]. The reduction in cell area and increase in efficiency with concentration enabled by this design may render III-V multijunction solar cells commercially viable for large-scale power generation.

Acknowledgment

The authors would like to thank Microscopy Australia for the facilities and the scientific and technical assistance at the Electron Microscope Unit within the Mark Wainwright

TABLE I
DESIGN PARAMETERS

Property	Value
$n_{polymer}$	1.564
w_{metal}	10.0 μm
p	40.0 μm
w_{trench}	12.0 μm
d	25.0 μm
h_{trench}	8.5 μm
h_{metal}	0.2 μm

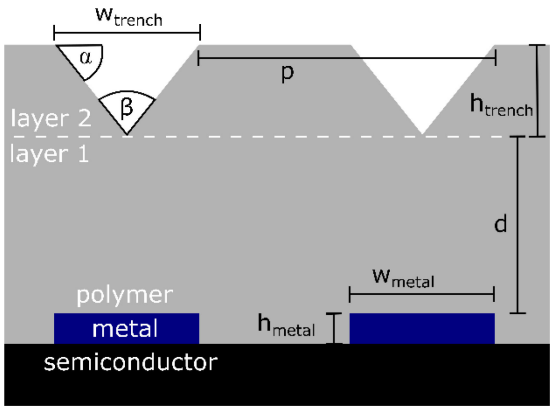

Fig. 8. Designed geometry and parameter labels (black). White labels are used to identify the different materials and to mark the interface between the first and second polymer layers (dashed white line).

Analytical Centre at UNSW Sydney. Responsibility for the views, information, or advice expressed herein is not accepted by the Australian Government. MPN acknowledges the support of the UNSW Scientia Program. This work is part of the research program of the Dutch Research Council (NWO).

APPENDIX

A. Methods

1) Design: The exact dimensions were subject to a few design constraints (see Fig. 8). The function of the patterned polymer layer relies on optical behavior that can be described by geometric optics. Therefore, the crosscut of the (symmetric) trenches needs to be at least a few microns in size to avoid influences from (sub-)wavelength-scale scattering effects. Second, the choice of the trench angles (top angle $\alpha = 54.7°$, bottom angle $\beta = 70.6°$) was fixed to be the same as the angles obtained from the (111) and (100) facets of silicon, which serves as the material for the master wafer. The separation between the tip/bottom of the trench and the metal contacts needs to be large enough to allow for all lights to be refracted away from the metal ($d_{\min} = \frac{w_{\text{metal}}}{2\tan(\gamma)}$), with γ being the angle at which light refracted from the trenches enters the polymer layer ($\gamma = 23.2°$). At the same time, the separation should not be too large so that the light is not refracted onto adjacent metal fingers ($d_{\max} = \frac{p - w_{\text{trench}}}{\tan(\gamma)}$). Here, w_{metal} was replaced with w_{trench}, as w_{trench} can be larger, to allow for some tolerance for alignment of the trenches and the metal contacts. The metal finger height h_{metal} is 200 nm, which is much smaller than any of the other dimensions and, hence, negligible in the optical design. Consequently, all dimensions involved follow directly from the choice of finger width w_{metal} and finger pitch p (see Table I).

2) Master and Stamp Fabrication: To achieve a well-defined geometry of parallel trenches, a 50 nm thick SiN_x mask was used. The SiN_x was deposited via plasma enhanced physical vapor deposition and subsequently patterned according to the desired trench width for the master wafer. This was done using AZ6632 photoresist in combination with photolithography. The patterned photoresist on top of the SiN_x served as a wet etch mask for HF (4.9%). For a sufficiently thin SiN_x layer, a wet etch with HF allows to break through the SiN_x in areas determined by the photoresist mask, without significant underetching. We used this SiN_x mask and a 20% KOH solution to etch down a (100) Si wafer. The SiN_x mask acted as an etch stop toward the edges and caused the initially random pyramids that are created by the KOH etch to merge into triangular (111)-plane trenches given sufficient etch time. Measurements from SEM images [see Fig. 3(b)] suggest that the actual achieved angle between wafer surface and trench wall is slightly smaller than the angle between the (100) and (111) planes, in line with recent investigation of scattering angles of pyramidal Si surfaces [32].

The fabrication of the PDMS stamp is described extensively by Verschuuren *et al.* [27] and we refer to that work for details. The only major difference is that Verschuuren *et al.* describe the stamp fabrication mainly in combination with Si masters that contain patterns of nanoscale objects, which do not change along the surface normal of the stamp. In our case, the fabricated structures are on the microscale and do change along the surface normal, but this does not influence the stamp fabrication, highlighting the universality of the approach.

3) Fabrication of Patterned Sample: To make the PDMS stamp compatible with the UV-lithography tool used for alignment and UV curing of the samples, the glass carrier onto which the PDMS mold is glued was diced to make the stamp fit into the tool. Furthermore, it was fixated onto a thick glass carrier to prevent it from breaking during fabrication. The UV-lithography tool used is a MBJ3 tool from SÜSS MicroTec with manual pressure control, which is beneficial when dealing with liquid photoresist as the range of applied pressure via the stamp can be monitored and adjusted more accurately than possible in some automated tools that focus on solid state UV lithography. For larger-scale application, the manual pressure control could be replaced by an automated pressure control system that stops upon contact with liquids. Before the imprint process, a 25 μm base layer of the transparent polymer (OrmoComp) is deposited via spin coating (30 s, 3000 r/min), heat cured (2 min, 80 °C), UV cured (1500 mJ/cm^2), and again heat cured (2 min, 80 °C). The second layer of the transparent polymer is prepared and processed at the same spinning and curing conditions to obtain the structure, as shown in Fig. 8.

Before UV exposure, the PDMS stamp is brought into contact with the liquid polymer layer on top of the sample in the UV-lithography tool. Once in contact, the stamp features and the metal finger lines on the sample are aligned with each other

to achieve the desired transparency. This alignment is done by using the attached optical microscope and comparing the position of the metal grid and trench lines of the stamp. During alignment the microscope is focused onto the plane containing the metal grid at low magnification. Higher magnification would mean that a greater range of incident angles is sampled, and hence, the fingers would appear nontransparent, even though they might be perfectly aligned with the trenches.

We found that a more general and effective method is alignment by minimizing the reflection by eye (making the sample appear as dark as possible). At the initial stage of the alignment, the orientation of trenches and metal contacts, which are usually not parallel to each other, leads to clearly visible Moiré patterns. The pattern alternates between dark and bright regions, which correspond to the absorber and metal reflection, respectively. By rotating the sample such that those regions become larger, and hence, the number of alternations across the sample less, the trenches and contacts are aligned in a parallel fashion. Next, the sample is translated such that the trenches and contacts are not only parallel but also on top of each other. This is visible by a change in brightness of the sample during translation, and the position for which the sample appears darkest corresponds to ideal alignment. We note that the simple alignment method described in this paragraph suggests that it should be fairly straightforward to transfer the procedure to the industrial scale.

For samples with front texture, this manual method is the only way of aligning the metal grid and the trenches, as the front texture scatters too much to be able to distinguish the metal covered area from the bare absorber in the microscope. This suggests that in a more advanced alignment setup, the alignment could work best by placing a light detector above the sample and minimizing the photon counts it receives. After exposure, the sample is carefully separated from the PDMS stamp and again heat cured as was done for the first layer.

4) Optical Characterization: The optical characterization was based on IS measurements. We used a Perkin Elmer Lambda1050 tool, along with its designated focusing and sample rotation kits. For reflection measurements, the sample was mounted behind the backside opening of the IS. An opening smaller than the sample was used, and the beam was focused such that it was also smaller than the opening. The distance between the focusing lens and sample was large enough to be able to assume that the range of AOI is negligible, and that the effective AOI was indeed 0°, with respect to θ. To measure the angular dependence of the absorption, the samples were fixed in the center of the IS, by using a designated holder clip. The holder clip can be rotated from outside the IS, which allows to vary the angle without having to reopen the tool. Furthermore, this measurement collects the sum of reflection and transmission. Hence, we assumed that all lights that were not collected were lost to absorption. Similar to the reflection measurements, the beam was focused onto the sample with a corresponding lens. Again, the distance between lens and sample was large enough to neglect widening of the range of AOI.

5) Angle-Resolved Reflection Measurements: These measurements (see Fig. 11) were conducted using an in-house custom built system [33] based at Macquarie University. The system uses a collimated supercontinuum laser as an illumination source that is passed through a Glan–Taylor prism to create the desired linear polarization. The illuminating light is then directed to reflect off the sample into a mini IS detector fiber coupled to a silicon or InGaAs charge coupled device (CCD) spectrometer. The system is configured in single beam configuration and is able to measure wavelengths in the range of 400–1800 nm. Measurements are taken sequentially, with a single measurement consisting of one AOI and one angle of reflection. The AOI for the illumination and the angle of detected reflected light are able to be independently changed across almost the entire range of 0°–90° relative to the samples normal.

6) Fabrication of the Si Solar Cells: An industrial 6 in silicon solar cell was obtained with a passivated emitter and rear cell (PERC) structure on the rear and SiN_x on the front. The cell was cleaved into 2×2 cm^2 pieces for the test structure. Photolithography was done on the front to remove parts of the passivation layer (with a buffered oxide etchant) and to create the desired Al fingers via evaporation, creating 1×1 cm^2 devices. The metal fingers are 10 μm in width with a pitch spacing of 40 μm, which correspond to 25% metal coverage. While the devices are not isolated on the wafer, this enables accurate measurement of the EQE.

7) Electronic Characterization: The EQE measurements were done with a PV measurements QEX7 system. The samples were brought into a focal spot with dimensions 1×4 mm. Samples were aligned such that the metal fingers were perpendicular to the light spot line.

B. Derivation of Effective Shading in (3)

Q_T is a function of the angular coordinate θ of the light source on a (hemi-)spherical surface with the solar cell located in the center, given by (2) from the main text. To obtain an angle average over the shading up to a certain maximum angle θ, we have to weigh $Q_T(\theta)$ by the surface area taken up by an infinitesimal slice of this hemispherical surface at the angle θ. Using a spherical coordinate system this amounts to

$$\begin{aligned}
S_{\text{eff}}\ (\theta) &= S\ \left(1 - \frac{\int dA\ Q_T\ (A)}{\int dA}\right) \\
&= S\ \left(1 - \frac{\int\int dx\ dy\ Q_T\ (x,y)}{\int\int dx\ dy}\right) \\
&= S\ \left(1 - \frac{\int\int r\ d\theta'\ r\cos(\theta')\ \ d\phi'\ Q_T\ (\theta')}{\int\int r\ d\theta'\ r\cos(\theta')\ \ d\phi'}\right) \\
&= S\ \left(1 - \frac{r^2 \int d\phi' \int d\theta' \cos(\theta')\ \ Q_T\ (\theta')}{r^2 \int d\phi' \int d\theta' \cos(\theta')}\right) \\
&= S\ \left(1 - \frac{\int_0^\theta d\theta' \cos(\theta')\, Q_T\ (\theta')}{\int_0^\theta d\theta' \cos(\theta')}\right) \\
&= S\ \left(1 - \frac{\int_0^\theta d\theta' \cos(\theta')\, Q_T\ (\theta')}{\sin(\theta)}\right) \\
&= S\left(1 - \frac{1}{\sin(\theta)} \int_0^\theta Q_T\ (\theta')\ \cos(\theta')\ d\theta'\right). \quad \text{(A1)}
\end{aligned}$$

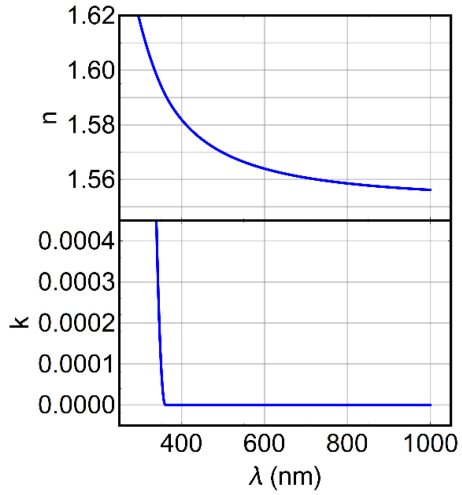

Fig. 9. Real (top) and imaginary (bottom) components of the refractive index of OrmoComp.

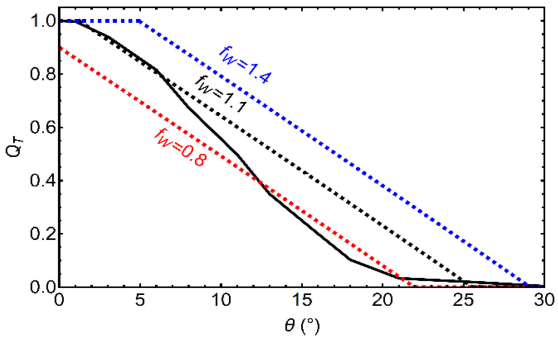

Fig. 10. Comparison of experimental angular dependence of Q_T (solid) and modeled dependences (dashed) for different values of f_W.

C. Optical Constants of OrmoComp

The optical constants of OrmoComp were determined using spectroscopic ellipsometry and by subsequently matching simulated and experimental reflection data for a film of 200 nm on top of a Si substrate. The data, as shown in Fig. 9, show a strong absorption onset around 360 nm, typical of UV photoresists.

D. Relevance of Ratio of Trench and Contact Width

The ratio of the widths of the trenches and the metal contacts determines the plateau width, as shown in Fig. 5(c), for which no performance loss at all is experienced with respect to θ. Fig. 10 illustrates this. The parameter f_W represents the ratio of the trench width to the contact width and is larger than 1 when the trenches are wider.

The experimental data correspond well with $f_W = 1.1$ up to $\theta = 8°$. Beyond that value, the experimental data show worse performance, which can be attributed to the fact that the modeled data do not take neighboring contacts into account, hence only describes the transparency for the contacts right under the trench. However, for increasing angle, refracted light rays may hit adjacent contacts. This contributes to a decrease in the experimental data beyond $\theta = 8°$.

The relevance of width ratio between trenches and contacts is also apparent from the figure. While trenches thinner than the contacts obviously let light pass onto the contacts, wider trenches lead to more resilience toward the AOI and, hence, suggest an improved performance as a function of angle. However, the discrepancy that we see between the experimental curve and the modeled data for $f_W = 1.1$ would already arise at angles below 8° as the trench is closer to the adjacent contacts.

E. Detailed Balance-Limit Calculations

To obtain the right *y*-axis, as shown in Fig. 7(a), the detailed balance limit [34] was calculated by balancing the generated current density [J_G, (A2)] with the recombination current density [J_R, (A3)], which yields an overall extracted current [J, (A4)]. The generated current density is a sum of the generation from sunlight (first term) and the received radiation from the ambient (second term, insignificant for the investigated bandgap range). Via iteration at different voltages, a current–voltage curve can be constructed from which short-circuit current density (J_{SC}), open-circuit voltage (V_{OC}), fill factor, and efficiency (η) can be predicted. By including a concentration factor (f_c), the calculation can be expanded toward concentrations different from 1 sun

$$J_G\ (E_{\mathrm{BG}}, f_c) = f_c\, q \int_{E_{\mathrm{BG}}}^{\infty} \phi_{\mathrm{AM1.5D}}\,(E)\, dE + \cdots + \left(\frac{f_{c,\max} - f_c}{f_{c,\max}}\right) q \frac{2\pi}{c^2 h^3} \int_{E_{\mathrm{BG}}}^{\infty} \frac{E^2}{e^{\frac{E}{kT}} - 1} dE \tag{A2}$$

$$J_R\ (E_{\mathrm{BG}}, V) = q \frac{2\pi}{c^2 h^3} \int_{E_{\mathrm{BG}}}^{\infty} \frac{E^2}{e^{\frac{E-qV}{kT}} - 1} dE \tag{A3}$$

$$J\ (E_{\mathrm{BG}}, V, f_c) = J_G\,(E_{\mathrm{BG}}, f_c) - J_R\,(E_{\mathrm{BG}}, V) \tag{A4}$$

where q is the electron charge, c is the speed of light in the vacuum, h is the Planck constant, k is the Boltzmann constant, T is the temperature of the solar cell (assumed to be at room temperature), and $f_{c,\max}$ is the maximum possible concentration. Furthermore, $\phi_{\mathrm{AM1.5D}}$ corresponds to the photon flux described by the AM1.5D solar spectrum, E_{BG} is the bandgap energy (set to 1.441 eV, which corresponds to GaAs), E is the energy of the incoming photon, and V is the applied voltage.

F. Angle-Resolved Reflection

Angle-resolved reflection measurements were conducted to confirm that the trench structure functions as intended, by refracting light into a specific angle, given by the trench angle. This was done for the same samples as in Fig. 5. We can see from Fig. 11(a)–(c) that the reflection angle that one would expect for light that is first refracted by the trench, then reflected by the sample, and finally out-coupled by the planar surface (dashed line) indeed matches well with the angle at which an intensity maximum is observed in the experimental data. There is a slight offset that could be related to a slightly different trench angle or refractive index of the fabricated sample. In general, the figure further confirms that the refractive behavior works as intended.

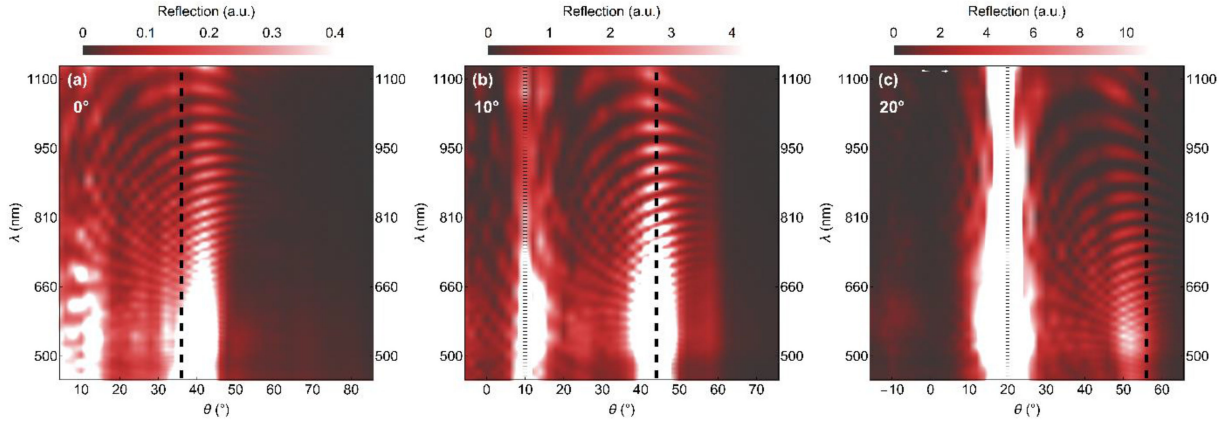

Fig. 11. Experimental data on reflected light intensity for specific receiving angles (θ) and wavelengths (λ). White corresponds to higher reflection intensity. (a), (b), and (c) correspond to angles of incidence of 0°, 10°, and 20°. The dashed line corresponds to the expected out-coupling angle for light that enters the sample via a trench and is out-coupled via a planar surface. The dotted line corresponds to the specular reflection of the incident beam.

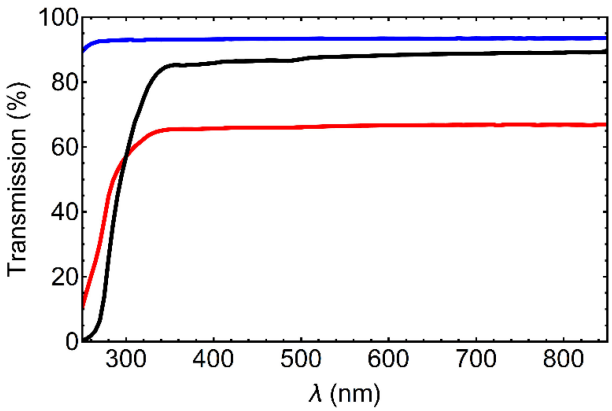

Fig. 12. Comparison of total transmission among a patterned quartz sample with Au grid (black), a planar sample with Au grid (red), and a bare quartz sample (blue). In this case, the metal (Au) coverage was 30%.

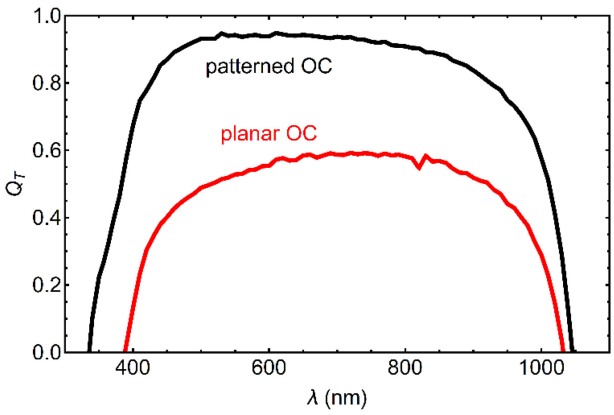

Fig. 13. Electronically derived Q_T as a function of wavelength, calculated using (A5). With the patterned case in black, and the planar case in red.

G. Transmission of Patterned Quartz Samples

Analogous to reflection measurements, transmission measurements were conducted using the IS. Fig. 12 shows the corresponding transmission spectra. In this case, the samples were mounted in front of the inlet of the IS, which is very close to the focusing optics of the setup, in comparison to the large optics sample distance for the reflection measurement. This means that the angular range of incident light was larger than the normal incidence that was sampled in the case of the reflection measurements. As a consequence, the patterned sample appears to perform worse in transmission than in reflection, as unfavorable, larger angles of incidence are sampled as well. Using (1) between 700 to 800 nm, we find $Q_T = 83.7\%$, for the transmission for this geometry.

H. Derivation of the Transparency From the EQE

For the quantification of Q_T in the electronic case, the peak value of the EQE of the patterned sample was used, and by taking reflection losses from the polymer into account, $Q_T = 94\%$ was calculated. This approach can be extended to the full wavelength range, although it assumes an ideal antireflection (AR)-coating effect, which is only true for the peak wavelength. Hence, Q_T is systematically underestimated for off-peak wavelengths. Fig. 13 shows the results that one would obtain using (A5) for the patterned case, but also for the planar polymer case, for which the light-trapping effect of the planar layer also yields Q_T values of up to 60%

$$Q_T\ (\lambda) = 1 - \frac{(1 - \mathrm{EQE}\,(\lambda) - (1 - f_g)\, r_{\mathrm{planar}} - f_g r_{\mathrm{patt}})}{f_m} \tag{A5}$$

where f_g is the fraction of polymer area covered with grooves, f_m is the fraction of solar cell area covered with metal, and r_{planar} and r_{patt} correspond to reflection from the planar and grooved polymer areas, respectively. It becomes apparent that this approach for calculating Q_T is only suitable for the range in which the combination of SiN AR coating and pyramidal texture is at an optimum.

REFERENCES

[1] L. Cozzi *et al.*, "World energy outlook 2020," Int. Energy Agency, Paris, France, 2020.
[2] E. Bellini, "Solar retains it LCOE edge in latest lazard analysis," *PV Mag.*, vol. 1, pp. 1–2, 2021.

[3] F. Uleman, V. Neder, A. Cordaro, A. Alù, and A. Polman, "Resonant metagratings for spectral and angular control of light for colored rooftop photovoltaics," *ACS Appl. Energy Mater.*, vol. 3, pp. 3150–3156, 2020.

[4] V. Neder, S. L. Luxembourg, and A. Polman, "Efficient colored silicon solar modules using integrated resonant dielectric nanoscatterers," *Appl. Phys. Lett.*, vol. 111, 2017, Art. no. 073902.

[5] R. A. Agathokleous and S. A. Kalogirou, "Status, barriers and perspectives of building integrated photovoltaic systems," *Energy*, vol. 191, 2020, Art. no. 116471.

[6] M. Heinrich *et al.*, "Potential and challenges of vehicle integrated photovoltaics for passenger cars," in *Proc. 37th Eur. PV Sol. Energy Conf. Exhib.*, 2020, pp. 1695–1700.

[7] S. Hubbard *et al.*, "Nanostructured photovoltaics for space power," *J. Nanophotonics*, vol. 3, 2009, Art. no. 031880.

[8] I. Cardinaletti *et al.*, "Organic and perovskite solar cells for space applications," *Sol. Energy Mater. Sol. Cells*, vol. 182, pp. 121–127, 2018.

[9] A. W. Y. Ho-Baillie *et al.*, "Deployment opportunities for space photovoltaics and the prospects for perovskite solar cells," *Adv. Mater. Technol.*, vol. 7, 2022, Art. no. 2101059.

[10] S. P. Philipps, A. W. Bett, K. Horowitz, and S. Kurtz, "Current status of concentrator photovoltaic (CPV) technology," Nat. Renewable Energy Lab., Golden, CO, USA, Tech. Rep. NREL/TP-5J00-65130, 2015.

[11] J. Aldersey-Williams and T. Rubert, "Levelised cost of energy—A theoretical justification and critical assessment," *Energy Policy*, vol. 124, pp. 169–179, 2019.

[12] S. P. Philipps and A. W. Bett, "III-V multi-junction solar cells and concentrating photovoltaic (CPV) systems," *Adv. Opt. Technol.*, vol. 3, pp. 469–478, 2014.

[13] H. J. Queisser, "Detailed balance limit for solar cell efficiency," *Mater. Sci. Eng., B*, vol. 159/160, pp. 322–328, 2009.

[14] J. F. Geisz *et al.*, "Six-junction III–V solar cells with 47.1% conversion efficiency under 143 suns concentration," *Nature Energy*, vol. 5, pp. 326–335, 2020.

[15] National Renewable Energy Laboratory, Best research-cell efficiency chart, 2021. [Online]. Available: https://www.nrel.gov/pv/cell-efficiency.html

[16] C. Amy, H. R. Seyf, M. A. Steiner, D. J. Friedman, and A. Henry, "Thermal energy grid storage using multi-junction photovoltaics," *Energy Environ. Sci.*, vol. 12, pp. 334–343, 2019.

[17] A. W. Blakers, "Shading losses of solar-cell metal grids," *J. Appl. Phys.*, vol. 71, pp. 5237–5241, 1992.

[18] M. F. Stuckings and A. W. Blakers, "A study of shading and resistive loss from the fingers of encapsulated solar cells," *Sol. Energy Mater. Sol. Cells*, vol. 59, pp. 233–242, 1999.

[19] M. F. Schumann *et al.*, "All-angle invisibility cloaking of contact fingers on solar cells by refractive free-form surfaces," *Adv. Opt. Mater.*, vol. 5, 2017, Art. no. 1700164.

[20] R. Saive *et al.*, "Silicon heterojunction solar cells with effectively transparent front contacts," *Sustain. Energy Fuels*, vol. 1, pp. 593–598, 2017.

[21] F. Chen, S. Pathreeker, J. Kaur, and I. D. Hosein, "Increasing light capture in silicon solar cells with encapsulants incorporating air prisms to reduce metallic contact losses," *Opt. Exp.*, vol. 24, pp. A1419–A1430, 2016.

[22] P. Jahelka, R. Saive, and H. A. Atwater, "Total internal reflection for effectively transparent solar cell contacts," 2016, *arXiv:1610.01047*.

[23] P. G. Kik, "Catoptric electrodes: Transparent metal electrodes using shaped surfaces," *Opt. Lett.*, vol. 39, pp. 5114–5117, 2014.

[24] R. Saive *et al.*, "Effectively transparent front contacts for optoelectronic devices," *Adv. Opt. Mater.*, vol. 4, pp. 1470–1474, 2016.

[25] C. H. van de Stadt, P. E. Gonzalez, H. A. Atwater, and R. Saive, "A computationally efficient simulation method for optimizing front contacts of concentrator multijunction solar cells," in *Proc. IEEE 46th Photovolt. Specialists Conf.*, 2019, pp. 288–291, doi: 10.1109/PVSC40753.2019.8980823.

[26] C. H. van de Stadt, P. E. Gonzalez, H. A. Atwater, and R. Saive, "A computationally efficient multidiode model for optimizing the front grid of multijunction solar cells under concentration," *J. Renewable Energy*, vol. 2020, 2020, Art. no. 1907530.

[27] M. A. Verschuuren, M. W. Knight, M. Megens, and A. Polman, "Nanoscale spatial limitations of large-area substrate conformal imprint lithography," *Nanotechnology*, vol. 30, 2019, Art. no. 345301.

[28] OrmoComp, *Micro resist technology*, 2022, Accessed: May 10, 2022. [Online]. Available: https://www.microresist.de/en/produkt/ormocomp/

[29] F. Rahman *et al.*, "A review of polymethyl methacrylate (PMMA) as a versatile lithographic resist—With emphasis on UV exposure," *Microelectron. Eng.*, vol. 224, 2020, Art. no. 111238.

[30] G. M. Giannuzzi, C. E. Majorana, A. Miliozzi, V. A. Salomoni, and D. Nicolini, "Structural design criteria for steel components of parabolic-trough solar concentrators," *J. Sol. Energy Eng.*, vol. 129, pp. 382–390, 2007.

[31] R. B. Diver and T. A. Moss, "Practical field alignment of parabolic trough solar concentrators," *J. Sol. Energy Eng.*, vol. 129, pp. 153–159, 2007.

[32] T. E. Scheul, E. Khorani, T. Rahman, M. D. B. Charlton, and S. A. Boden, "Wavelength and angle resolved reflectance measurements of pyramidal textures for crystalline silicon photovoltaics," *Prog. Photovolt.*, vol. 28, pp. 1248–1257, 2020.

[33] D. N. R. Payne, M. D. B. Charlton, and D. M. Bagnall, "Broadband wavelength and angle-resolved scattering characterization for nanophotonics investigations," *Appl. Opt.*, vol. 54, pp. 7224–7229, 2015.

[34] W. Shockley and H. J. Queisser, "Detailed balance limit of efficiency of p-n junction solar cells," *J. Appl. Phys.*, vol. 32, pp. 510–519, 1961.